Materials and Structures (2008) 41:1169–1189
DOI 10.1617/s11527-007-9316-z

ORIGINAL ARTICLE

Evaluation of the repair on multiple leaf stone masonry by acoustic emission

Anna Anzani · Luigia Binda · Alberto Carpinteri · Giuseppe Lacidogna · Amedeo Manuello

Received: 17 November 2006 / Accepted: 20 September 2007 / Published online: 24 October 2007

Abstract Aim of this research was to evaluate the possible application of the AE technique to study the response of multiple leaf masonry repaired with different techniques. The results of shear tests carried out on three specimens repaired after failure are presented on an explorative basis; on two of them the acoustic emission (AE) technique was also used. Through a number of sensors and by triangulation, this technique makes it possible to identify the location of the damage, unknown initially, and subsequently to assess the stability of its evolution. Using the AE technique the area of the material where the cracks propagated during shear tests was identified. These analyses made it possible to evaluate the effectiveness of repair interventions through parameters other than stress and strain, and contributed to the identification of the most suitable methodology for their optimisation.

Keywords Multiple-leaf masonry · Grout injections · Shear response · Acoustic emission technique · Damage localisation

A. Anzani · L. Binda
Department of Structural Engineering,
Politecnico di Milano, Milan, Italy

A. Carpinteri (✉) · G. Lacidogna · A. Manuello
Department of Structural Engineering and Geotechnics,
Politecnico di Torino, Corso Duca degli Abruzzi, 24,
Torino, Italy
e-mail: alberto.carpinteri@polito.it

1 Introduction

Most historical centres in Italy are characterised not only by the presence of monumental buildings such as churches and palaces, but also by a man-made environment, which in itself constitutes an important part of the cultural heritage. Both monumental and minor architectural structures are often made of stonework masonry and were built using different techniques depending on pre-existing elements, social and economic factors and local sources. In most cases they are made of the so called multiple leaf stone masonry, the specific characteristics of which should be understood before undertaking a safety assessment on many kinds of structures. This is the case, for instance, when considering the seismic vulnerability of stonework buildings, but it also applies to the evaluation of the stability of ancient cathedrals, whose pillars have non-homogeneous cross-sections.

An experimental research was previously carried out on 12 three-leaf walls built using two stones having different characteristics, and according to two geometric patterns (with and without stone offsets) in order to guarantee different degrees of connection between the leaves, in an attempt to reproduce two masonry types frequently used in Italian historical city centres [1, 2]. The aim of the research was to understand the stress-strain behaviour of this masonry under compression and shear actions and to evaluate the possibility of interpret it by analytical modelling.

After shear testing, three specimens could be recovered and repaired by grout injections and steel rods confinement and on two of them the AE was applied to monitor the damage development during the tests. The mechanical properties of multiple leaf stone masonry walls vary as a function of the types of stone used and the strengthening methods adopted, and hence the cases illustrated are not sufficient to perform a statistical analysis of the mechanical behaviour of these walls. However, albeit still tentative, the purpose of the present stage of the research is to gain an initial comparative knowledge on the repair techniques adopted, to explore the suitability of the AE technique for the interpretation and evaluation of their effectiveness and its capacity to capture the different characteristics of the walls analysed.

For the localisation of damage, a sophisticated equipment for the analysis of AE signals was used during laboratory tests on two of the test pieces repaired. This equipment consists of six USAM® units for signal acquisition and processing. Each of these units analyses in real time, and transmits to a PC, all the characteristic parameters of an ultrasonic event. In this manner, each AE event is identified by a progressive number and characterised by a series of data giving the amplitude and the time duration of the signal and the number of oscillations. Moreover, the absolute acquisition time and signal frequency are also given, so that, through an analysis of signal frequency and time of arrival at the transducers, it is possible to identify the group of signals belonging to the same AE event and to localise it. Each unit is equipped with a pre-amplified wide-band piezoelectric sensor (PZT), which is sensitive in a frequency range of between 50 kHz and 800 kHz. The signal acquisition threshold can be set in a range of between 100 μV and 6.4 mV. As it is known, the cracking process inside the material subjected to compression and shear takes place through the formation of a quantity of microcracks. With increasing loads, these coalesce into macrocracks, whose formation brings about a reduction in the bearing capacity of the structures [3–5]. The statistical techniques derived from seismology, such as the Gutenberg-Richter (GR) law, related to AE monitoring, clarify the relationships between microstructural events and the macroscopic behaviour of structures during the damaging process [6–8].

2 Specimen preparation

Twelve three-leaf stone walls, measuring $310 \times 510 \times 790$ mm^3, were built at DIS—Politecnico di Milano, by Spadaro srl Contractor—Rosolini, Sicily, so as to reproduce the morphology of the multiple-leaf walls and piers frequently encountered in historical centres (Figs. 1 and 2). The two external leaves, made of stone blocks with horizontal and vertical mortar joints, are connected to an internal rubble masonry leaf made of pebbles of the same kind of stone and connected with the same mortar as the outer leaves [1]. The experimental investigation was aimed to study the compression and shear response of the interface between the masonry leaves so as to achieve some understanding of the bearing capacity of the structure after perfect mutual collaboration has been lost due to a non-uniform vertical action or in-plane horizontal forces.

Fig. 1 Phases of construction

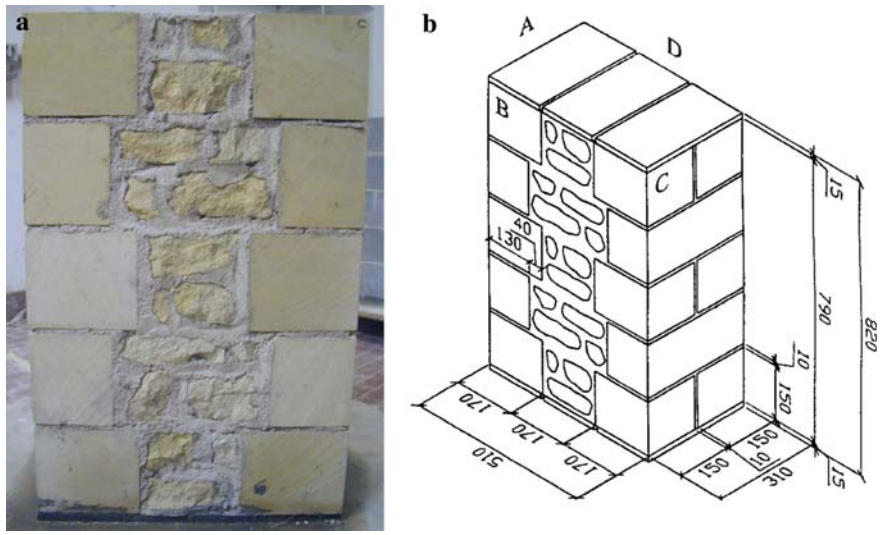

Fig. 2 Typical geometry of the tested walls

A ready-to-mix hydraulic lime mortar was used to build both the external and the internal leaves of all the masonry specimens. During the construction of the masonry walls, mortar specimens sized $40\times 40\times 160$ mm^3 were prepared for testing according to EN 1015-11, CEN 1999 after different curing times (28, 70, 90, 175 days) as indicated in Table 1. The mechanical characteristics of the mortar are given in Table 1.

In order to investigate the influence of stone on the behaviour of the wall, two types of stones were chosen: the same limestone used for the Noto Cathedral (Noto stone) and a sandstone, frequently used in central and southern Italy (Serena stone). The characteristics of the two stones were obtained on cylindrical specimens, 80 mm in diameter and 160 mm high, cored from regularly cut stones. Physical characteristics were determined by means of the dry, saturated and hydrostatic weight, and are reported in Table 2, together with the mechanical characteristics. Compressive strength (σ_c) was determined in both directions, normal and parallel to the bedding planes, and tensile strength (σ_t) was determined in the same direction as the bedding planes. The values of the elastic modulus (E_a) and Poisson's ratio (v_a) have been determined as an average over three specimens. It is quite evident that the Serena stone exhibits a higher density (γ_b) and a lower value of porosity (P_o) than the Noto stone; accordingly, also the compressive and tensile strength values are higher.

Table 1 Characteristics of the mortar

Age [days]	σ_t [N/mm^2]	σ_c [N/mm^2]	E [N/mm^2]
28	1.53	7.54	2.475
60	–	–	3.389
75	1.97	9.34	–
90	2.39	9.84	–
175	2.27	11.37	–

Table 2 Characteristics of the stones

Stone	γ_b [kg/m^3]	P_o [%]	Load versus bedding planes direction	σ_c [N/mm^2]	E_a [N/mm^2]	v_a	σ_t [N/mm^2]
Noto	1730	15.4	Normal	20.6	9476	0.10	2.06
			Parallel	17.6	8526	0.09	–
Serena	2538	2.1	Normal	104.2	18218	0.19	6.07
			Parallel	89.0	23293	0.21	–

3 Shear tests before and after repair

Eight walls were tested to failure in shear conditions according to the loading scheme shown in Fig. 3. Further details on the complete experimental work can be found in [2, 9].

After the shear tests, the Serena stone specimens presented an average peak load about 1.5 times higher than the Noto stone specimens due to the higher strength of the stones. Many vertical and sub-vertical cracks diffused in the inner leaf could be detected. In the case of the Noto stone specimens, such cracks often cut the stones (Fig. 4), whereas in the case of the Serena stone specimen cracks tended to propagate in the mortar at the interface with the stone fragments.

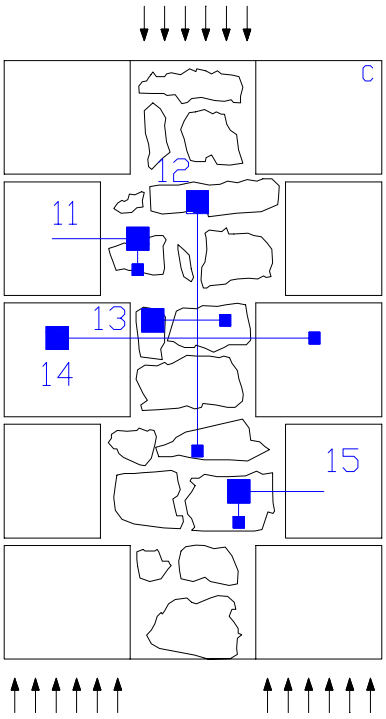

Fig. 3 Loading condition

This is probably due to two reasons: the lower strength of the Noto stone; the better adhesion that can be assumed between the mortar and the Noto stone, given its high porosity, as shown in Table 2. In fact, it is well known that adhesion results from a chemical–physical process that starts when mortar is still fresh, takes place during the curing phase, and is based on water evaporation and carbonation. It is strongly influenced by different factors including the moisture retentivity of the mortar, the grading of its sand, the roughness of the stones surface, their initial rate of suction, their moisture content at the moment of laying [10], their porosity. In relative terms, comparing the Noto stone and the Serena stone, being the mortar the same, the higher the porosity and the water absorption by the stone, the better the expected adhesion between mortar and stone. The outer leaves in the case of the Noto stone, suffered from some cracks that opened at the base of the specimens.

Once removed from the testing machine and stored in the laboratory, three walls were repaired and subsequently tested again. Before repairing the walls by injection, a partial reconstruction of the outer leaves was necessary as can be seen in Fig. 5a. The repair was carried out by means of grout injections designed to fill the main cracks formed at the interface between the inner and the outer leaves during the test [11–13] and by fitting steel bars. In particular, completely inorganic mixes based on microfine pozzolanic binders (Fig. 5) were used [14–16] and rods, having a diameter of 16 mm and characterised by an elastic modulus of 19500 N/mm^2,

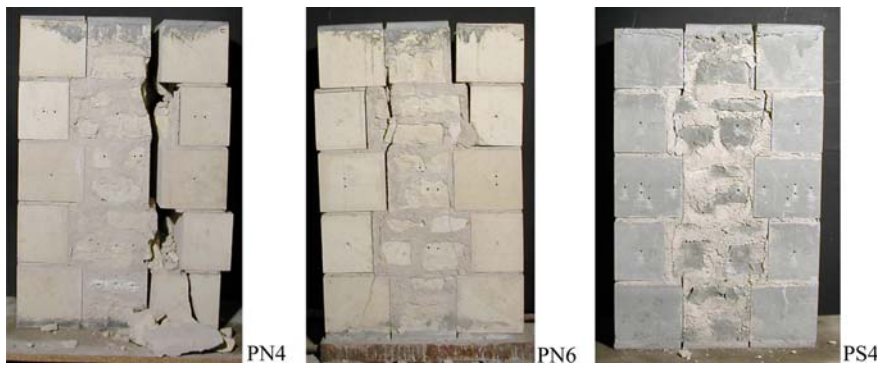

Fig. 4 Appearance of the specimens once removed from the testing machine

Fig. 5 Injections in the walls

were applied by tightening the nuts to a torque of 50 Nm (Fig. 6). This corresponds to a longitudinal action of 15.63 kN on each rod, corresponding in its turn to a total lateral confinement on each wall of 0.37 N/mm^2.

The characteristic values reached through the shear tests before and after the repair and the techniques adopted to repair the specimens are indicated in Table 3. The results of the tests on the repaired specimens can be seen in Figs. 7–9, where the load versus displacement diagrams are shown, compared to those obtained on the virgin specimens.

Fig. 6 Wall repaired with steel rods

The repair always caused an increase in load-bearing capacity, expressed in Table 3 as the ratio between the maximum load sustained by the repaired wall and that sustained by the virgin wall. As shown in the table, the increase was found to be 1.24 times as great in the case of specimen PS4, in Serena stone repaired by grout injections only, and even more appreciable in the other cases.

In the two cases where the repair was made through injections (PS4 and PN4), the subsequent collapse of the two collar joints, that could be clearly observed in the diagrams plotted before the repair, is no longer visible. This is still scarcely evident in the case of the wall repaired only with steel rods (PS6), in which case the diagram shows a small decrease, corresponding to a displacement of 6000 μm (Fig. 8).

In the case of specimen PS4, the diagram plotted after the repair repeats the same trend observed before the repair in the branch preceding the failure of the first collar joint and maintains this slope until failure. From a qualitative point of view, the behaviour is more brittle than that of wall PS4 before the repair (Fig. 7).

Only in the case of specimen PS6, a very ductile and markedly compliant behaviour can be observed

Table 3 Characteristics of the walls tested before and after repair

Wall	Repair	Virgin		Repaired		$P_{max,r}/P_{max,v}$
		$P_{max,v}$ [kN]	$\delta_{max}[\mu m]$	$P_{max,r}$ [kN]	$\delta_{max}[\mu m]$	
PS4	Injection	391.10	4056.84	485.33	2971.91	1.24
PS6	Steel rods	415.89	4369.80	700.88	8462.52	1.68
PN4	Injection and steel rods	283.35	2633.31	520.17	6636.51	1.83

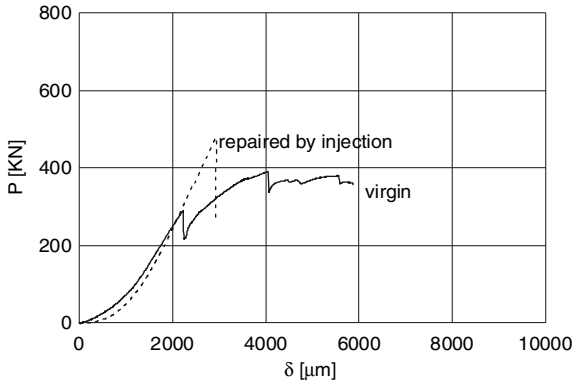

Fig. 7 PS4 in Serena stone

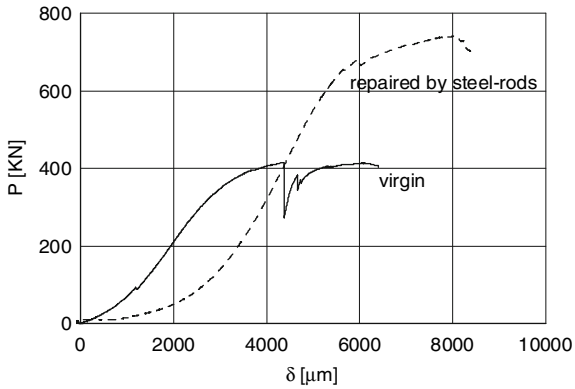

Fig. 8 PS6 in Serena stone

even after the repair (Fig. 8). This last aspect is probably due to the presence of previous cracks that had not been filled and that, in the initial part of the test, allowed a relative displacement between the inner and the outer leaves. The great ductility of the failure behaviour is probably due to the friction developed at the interface between the three leaves induced by the load from the steel rods, combined with the characteristics of the stone. In fact, the Serena stone is characterised by a higher mechanical strength and, in the presence of lateral confinement, the stones of the outer leaves do not reach locally the failure values, as can be gathered from the crack pattern discussed below. Therefore, on the whole, failure is governed by the rupture of the inner leaf that overall displays a scarcely brittle behaviour.

Conversely, in the case of specimen PN4, repaired with both steel rods and injection, the behaviour is less brittle than that of PS4, but also less ductile than

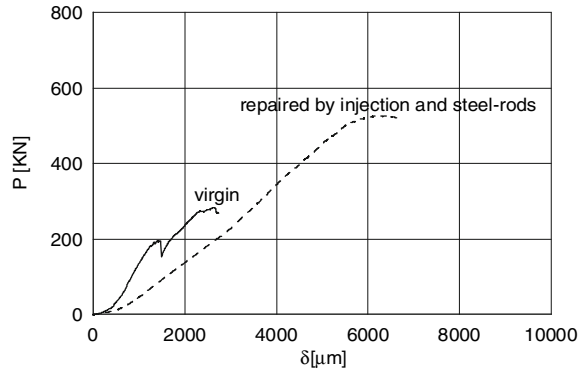

Fig. 9 PN4 in Noto stone

that of PS6, indicating an involvement of the outer leaves at failure, as confirmed by the crack pattern described below. This is probably due to the lower strength of the Noto stone and to the very good collaboration between inner and outer leaves produced by crack filling. In fact, in the case of specimen PN4, a reduction in the elastic modulus compared to the virgin situation and a brittleness similar to that observed in PS4 have to be highlighted, such that the diagram maintains the same slope until failure; this is probably related to the effect of closing the cracks and re-gaining the continuity given by the grout injection.

From an analysis of the crack patterns (Figs. 10–12), what is seen in the diagrams can be confirmed. In addition, a comparison with the crack pattern of unrepaired prisms can be made: the tests carried out after the repair resulted in the same cracks opened previously opening again and new ones being formed.

In particular, in the case of prism PS4 (Fig. 10), the tendency to diagonal load diffusion, the collaboration between the inner and outer leaves due to grouting, and the absence of lateral confinement led to the failure of a stone block, at the base of the outer leaf.

In the case of specimen PS6 (Fig. 11), the most ductile one because of the steel rods and the quality of the stone, the outer leaves did not crack. Failure took place through cracks in the inner leaf mostly involving the mortar at the interface with the stone pebbles, and at the interfaces between the inner and the outer leaves; cracks also propagated diagonally indicating the load diffusion and, on face D, presented a concentration with detachment of

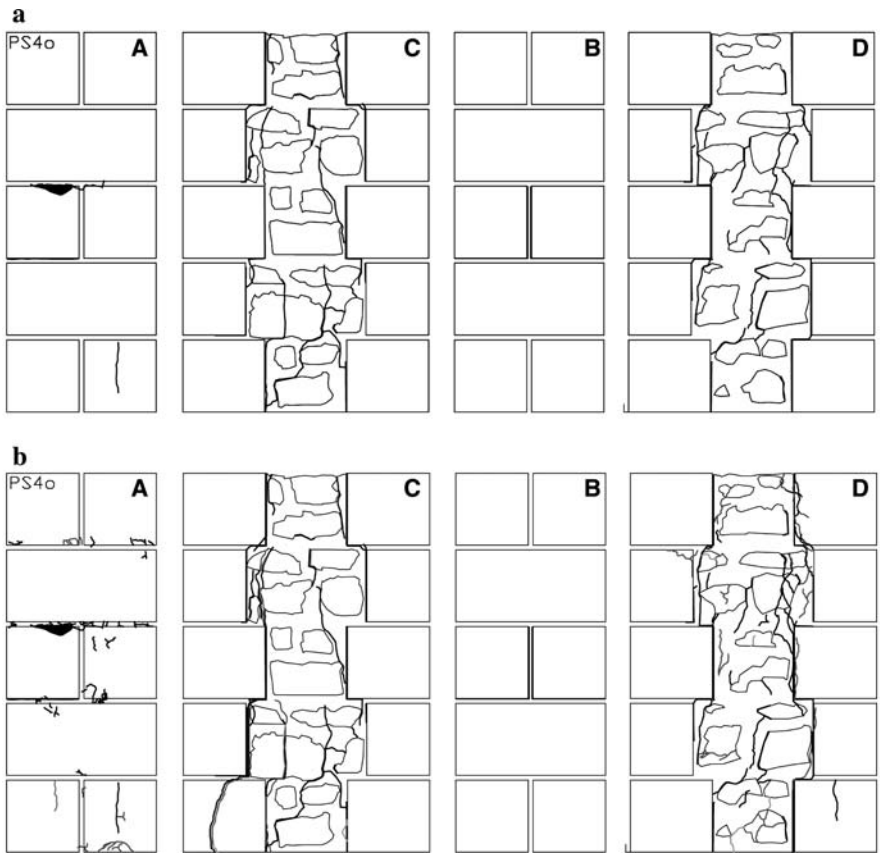

Fig. 10 Crack pattern in wall PS4 before (**a**) and after (**b**) repair

material corresponding to the second stone layer from the top.

In the case of specimen PN4 (Fig. 12), a greater involvement of the outer leaf took place at failure, when new cracks opened and, in some areas, delamination occurred, together with the propagation in the inner leaf of cracks that sometimes also cut the stone pebbles. In this case horizontal cracks were also visible, both on the outer leaf and on the inner leaf at the base level, due to the compression effect produced horizontally by the presence of the steel rod during the loading phase, given the low strength of the stone.

Figures 13a–15a show the shear stress versus strain diagrams obtained from the readings of single LVDTs (Linear Variable Displacement Transducers) placed as shown in Figs. 13c–15c, whereas Figs. 13b–15b show the load versus relative displacement diagrams from LVDTs placed at the interface between inner and outer leaves. Conventionally, shortening was plotted as positive and elongation as negative; apart from some anomalous readings indicated below, vertical strains are always positive and horizontal ones are always negative.

As can be seen in Figs. 13a, 14a, 15a, vertical strains observed in the inner leaf show higher values than those obtained on the outer leaves, obviously due to the load application method. In the case of wall PS4 (Fig. 13b), significant relative displacements can be observed relatively to LVDT 11, placed in a higher position, probably due to a low adhesion between Serena stone (having very low porosity) and grout; to the contrary, in the case of LVDT 12, a shortening effect, indicating no relative displacements, was mainly observed.

The situation is very different in the case of wall PS6, repaired only with steel rods. In this case, both LVDTs reading the relative displacement (numbered as 10 and 12 in Fig. 14b) recorded considerable values, higher than those recorded for the other walls. This is consistent with the presence of cracks at the interface that had not been filled, since the wall was not injected. Vertical relative displacements along the cracks at the interface between

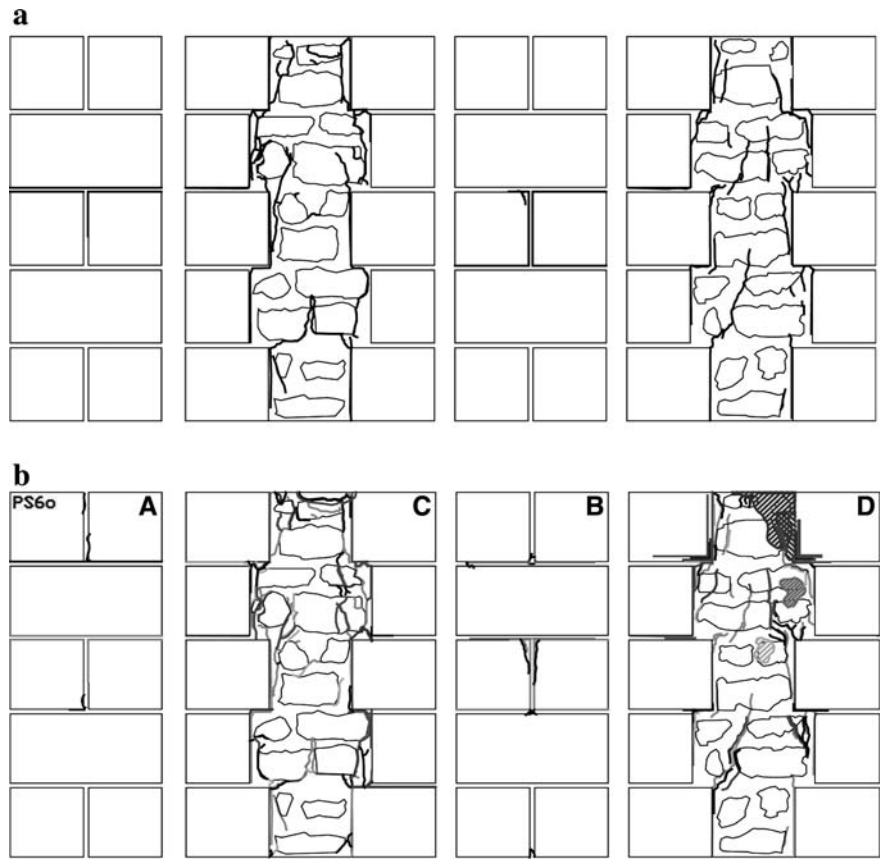

Fig. 11 Crack pattern in wall PS6 before (**a**) and after (**b**) repair

inner and outer leaves can also explain the very ductile behaviour shown in Fig. 8 and commented previously.

In the case of wall PN4 only LVDT 5, having a longer basis, shows higher readings than the other vertical ones, whereas all the other vertical LVDTs show very similar strains. This indicates that, in the case of Noto stone, which is characterised by a high porosity, a good adhesion probably developed, as borne out by the first test series [2], which resulted in similar strains in the inner and outer leaves, with essentially no relative displacements at the interface. This is also confirmed in Fig. 15b by the virtually nil readings from LVDT 3. The readings from LVDT 4 do not indicate a relative displacement mostly because, given the considerable length of the bases of the transducer, they are influenced by the shortening effect of the inner leaf. Moreover, the presence of the steel rods probably played a role in reducing the displacements, given the contribution of frictions. Anomalous readings from LVDTs 2, 8 and 11 in Fig. 15a are probably due to a lateral bulging of the layer not confined by the steel rods.

4 Application of the acoustic emission technique

Acoustic emissions are ultrasonic waves generated by a rapid release of energy, coming from discontinuities or cracks propagating in materials subject to states of stress or strain. In isotropic and homogeneous materials, the waves propagate through the solid, according to straight rays moving at the same velocity v in every direction, until they reach the outer surface, where they are captured by ad hoc sensors [4–6]. If the solid is damaged or inhomogeneous, propagation velocity and frequency tend to vary progressively during the cracking process, and the range of these two parameters can be determined only through experimental techniques [17–19]. The process is similar to the one that takes place in seismology, where the elastic waves generated by the

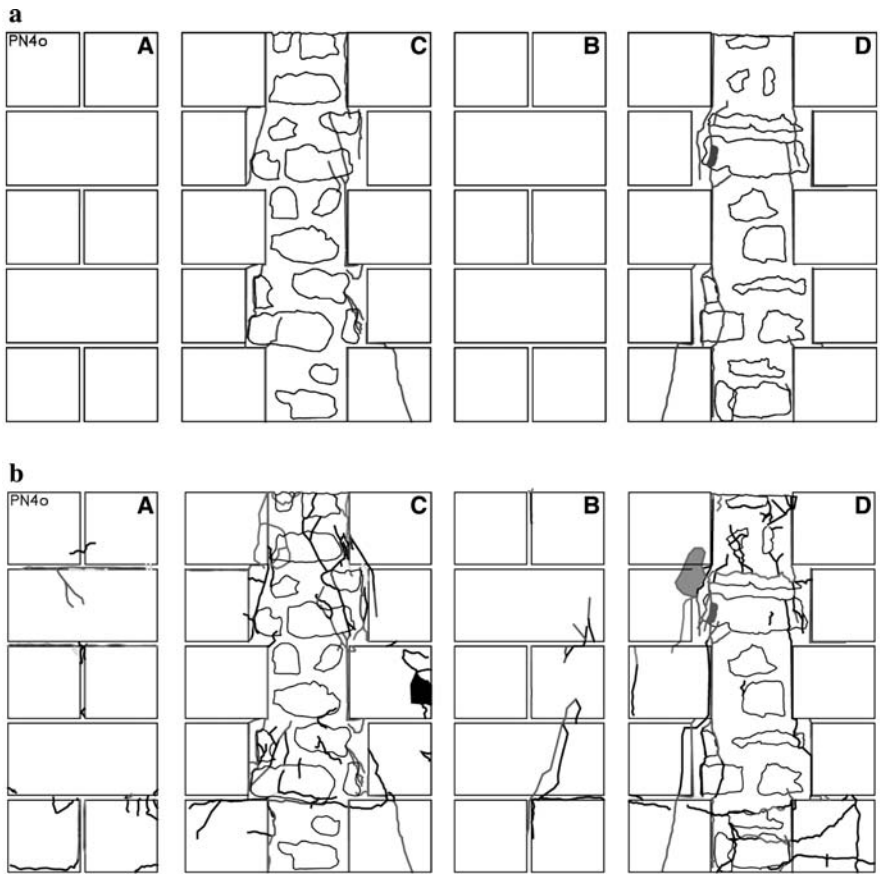

Fig. 12 Crack pattern in wall PN4 before (**a**) and after (**b**) repair

earthquakes reach the monitoring stations positioned on the surface of the earth [7].

Though it finds its theoretical foundations in the laws of physics on elastic wave propagation, with appropriate assumptions and limitations the Acoustic Emission technique can be applied to the analysis to heterogeneous solids [17, 18]. AE events consist of wave trains whose initial part is made of longitudinal waves (P) and shear waves (S), and the remaining part is given by the superposition of surface waves and that fraction of indirect waves arriving later due to the multiple reflections present in all materials [20]. In many instances it is not easy to discern the source of AE events. This is due to the temporal superposition of different processes associated with the propagation of the waves in a medium, including secondary events, such as reflections, and the attenuation of their width along their path.

According to elastic wave theory, propagation velocities only depend on the density the modulus of elasticity and the Poisson's ratio of the material. However, in heterogeneous solids, when a wavefront produced by an AE generating microcrak meets a discontinuity in the elastic properties of a material—a condition that occurs at the surface of separation between two media having different propagation velocities—a portion of the energy is reflected and remains in the first medium and another portion is transmitted by refraction into the second medium. The laws governing reflection and refractions are based on Huygens' principle according to which a wavefront can be regarded as the envelope of many elementary wavefronts generated by particles that are made to vibrate by the effects of the wavefront in the previous position. As a result, the wavefront propagates in a material in which either spherical or conical wavefronts will be generated depending on the propagation velocities of the waves in the propagation surfaces.

Obviously, the geometric divergence in signal localisation is caused primarily by the enlargement of the wavefront, which essentially depends on the

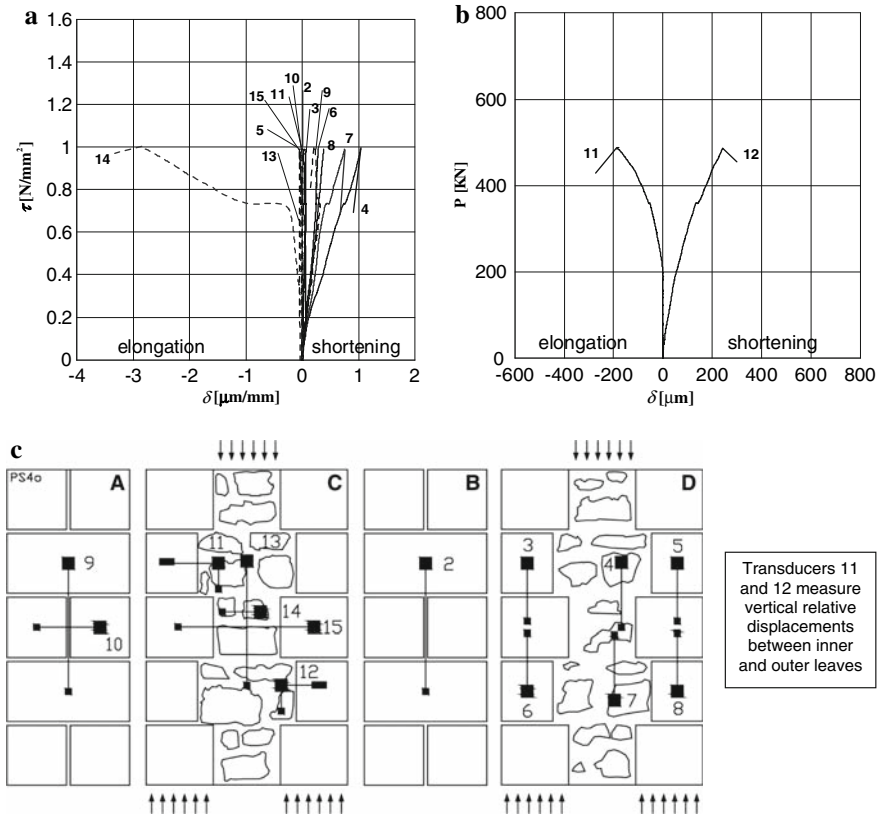

Fig. 13 Results in wall PS4

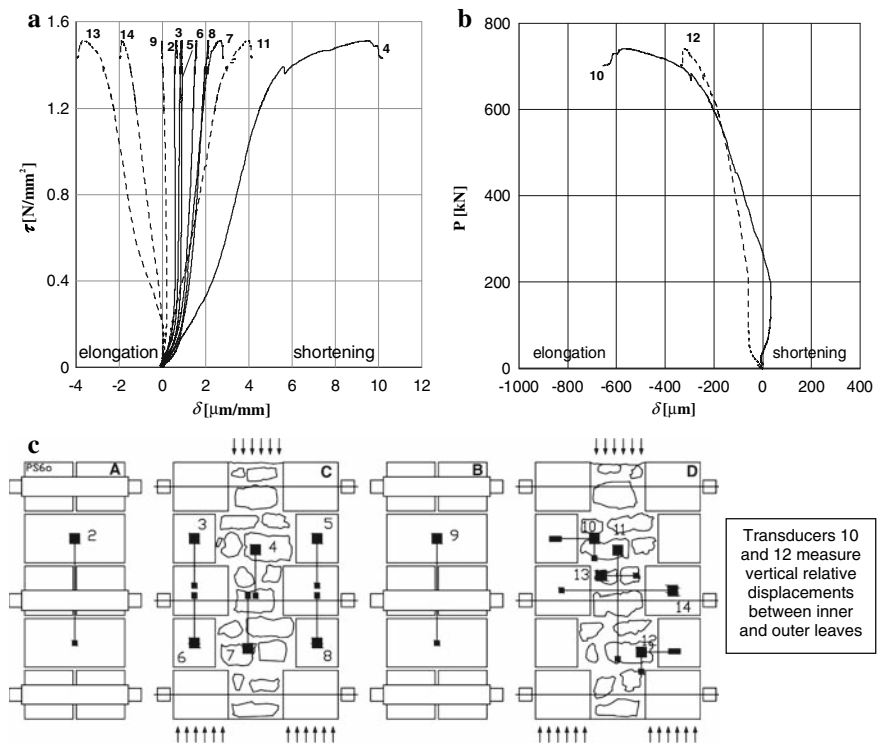

Fig. 14 Results in wall PS6

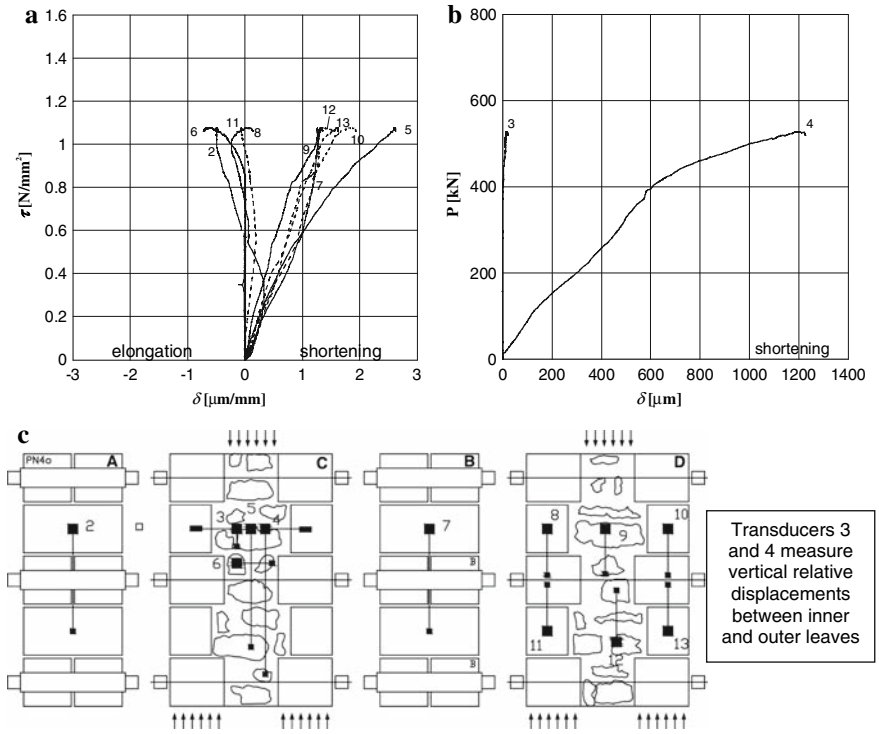

Fig. 15 Results in wall PN4

inhomogeneity of the material. It could be estimated by considering a model of wave propagation in the material between the AE source and the individual transducers. Yet, on account of the complexity of the problems, it is common practice to quantify signal localisation errors empirically, by comparing the source localised through the AE technique with the one identified visually in the specimen analysed [20]. An alternative procedure consists of trying to identify an average transmission velocity of the waves in the medium and determining the influence of the angle of incidence on signal reception by the transducers using an artificial source produced by breaking the tip of a pencil on the outer surface of the material [17, 19].

In this paper, as described in Sect. 4.1, six transducers have to be employed to determine the unknown source time, the average transmission velocity of AE signals in the medium and the three source coordinates in an univocal way. By applying a least squares approach, time residuals at the different transducers are calculated and random measurement errors can be recognised. Mean residuals correspond to the theoretical accuracy of the localisation result [21, 22]. With this localisation procedure, though the materials analysed with the AE technique are indubitably heterogeneous, they are assumed to be homogenous and isotropic in the sense of being characterised in every direction by an average transmission velocity of the waves [19].

As for material attenuation properties, it is known that they depend on the frequency range: higher frequency components propagate in materials with greater attenuation. Moreover, for heterogeneous materials such as masonry or concrete, additional attenuation due to dispersion at the internal interfaces and dissipation of energy occurs. It depends on the material's properties and frequency content, and can be quantified only empirically. It is reasonable to assume that, for wave propagation through a heterogeneous material, the frequency dependent attenuation must be in some way a function of the degree of heterogeneity. If the size of the largest inhomogeneity is used to characterise the material, then the wavelength needs to be larger than that of the maximum inhomogeneity in order for the wave to "pass through" without significant modifications in its waveform [18].

In the testing program described in this study, as we shall see in Sect. 5, the average velocities

measured in the multiple leaf stone masonry specimens ranged from 980 to 1350 m/s, while average frequency was seen to range from 90 to 120 kHz, respectively. Based on the measured velocity of P waves, these frequencies correspond to wavelengths of 10.9 and 11.25 mm. Though maximum-sized inhomogeneities in stone and mortar are not perfectly known, surely they are no bigger than a few mm in diameter. Moreover, by analogy with the results of tests performed according to the US wave technique [18], it can be assumed that the size of entrapped air bubbles in the materials making up the test pieces is a few hundred micrometres in diameter. Hence the wavelengths observed would surely be able to pass through the discontinuity with a slight attenuation of the AE signal, as borne out by the results of the tests described in this paper.

Obviously, also on account of the limited quantity of data available on masonry elements in the international literature, these considerations, albeit validated by the results of the tests, should be supported by further statistically significant measurements. In this manner, the parameters governing the propagation of ultrasonic waves in multiple leaf stone masonry specimens as a function of mortar composition and type of stone used could be defined with greater accuracy. The goal is to be able to foresee the evolution of damage in this type of masonry, both in the laboratory and during on-site monitoring, or in order to assess the effectiveness of strengthening interventions [3, 5, 11].

From the foregoing it can be inferred that the AE technique is the only structural monitoring method able to identify damaging phenomena during their evolution. The waves emitted are physically identical to seismic waves; transient AE waves of feeble amplitude are characterised by high-frequency components in the ultrasonic range. In the theoretical development of AE, Ohtsu and Ono summarised the theoretical treatment as a generalised theory of AE [23], which essentially follows the representation theorems of seismic sources shown by Maruyama, Aki and Richards [22–24]. While in seismic analysis the mechanism investigated by seismologists mostly consists of the mutual sliding of the faults, in structural monitoring through the AE technique, the elements subjected to different loading conditions in the laboratory and in situ differ primarily from earthquake studies in the presence of tensile cracks. AE theoretical approach includes not only shear dislocation but also tensile dislocation [23].

4.1 Localisation of acoustic emission sources

As mentioned in the Introduction, the equipment used by the authors consisted of six USAM® units for AE signal acquisition and processing. The equations used for source localisation are based on the assumptions of a homogeneous and isotropic medium and point-like sources, entailing spherical wave propagation. Generally speaking, for single point-like sources in geometries having continuous straight paths between the source and each receiver, the localisation technique is called "triangulation procedure". During the first stage, the groups of signals, recorded by the various sensors, that fall into time intervals compatible with the formation of microcracks in the space analysed, are identified. These time intervals, of the order of micro-seconds, are defined on the basis of the presumed speed of transmission of the waves (P) and the mutual distance of the sensors applied to the surface of the material.

It is usual to assume that the amplitude threshold of 100 μV of the non-amplified signal is appropriate to distinguish between P-wave and S-wave arrival times. In fact, P-waves are usually characterised by higher value signals [20, 25, 26].

In the second stage, when the formation of microcraks in a three-dimensional space is analysed, the triangulation technique can be applied if signals recorded by at least five sensors fall into the time intervals. Thus, with this procedure it is possible to define both the position of the microcracks in the space and the speed of transmission of P-waves. Having denoted with t_i the time of arrival at a sensor S_i of an AE event generated at point S at time t_0, $|S - S_i| = [(x - x_i)^2 + (y - y_i)^2 + (z - z_i)^2]^{1/2}$, the distance between S_i and source S, in Cartesian coordinates, and assuming the material to be homogenous (in the sense explained in Sect. 4), the path of the signal is given by: $|S - S_i| = v(t_i - t_0)$. If the same event is observed from another sensor S_j at time t_j, it is possible to eliminate t_0 from the equation:

$$\left|S - S_j\right| - |S - S_i| = v(t_j - t_i) \equiv v\Delta t_{ji}. \quad (1)$$

Assuming the arrival times of the signals and the positions of the two sensors to be known, Eq. 1 is an

equation with four unknowns, x, y, z and v. Hence, the localisation of S is a problem that can be solved in an exact manner if it is possible to write a sufficient number of equations such as Eq. 1, i.e., when an AE event is identified by at least five sensors. If this did not occur, it would be necessary to adopt simplifying assumptions to reduce the degrees of freedom of the problem, such as, for instance, imposing the speed of transmission of the signals or having the AE source lie on a plane of predetermined coordinates. The localisation procedure can also be performed through numerical techniques using optimisation methods such as the Least Squares Method (LSM) [21]. The LSM is used to estimate the source location that minimises the sum of all squared time residuals. The non-linear system involved during LSM method is usually solved using iterative techniques with algorithms based on Gauss–Newton's method usually adopted in Seismology [21, 22].

4.2 Moment tensor analysis

Damage can be considered from the microscopic standpoint as consisting of a succession of discrete events, localised in space and time. They develop at different times in the parts of the structure where stresses are highest. Having identified the individual AE events through the localisation process, it is interesting to evaluate the orientation, the direction and the modalities of the microcracks. Moment tensor analysis was developed in seismology to describe the mechanics of earthquakes. The same method, transferred to the field of acoustic emissions is able to represent a source of ultrasonic waves in terms of motion and orientation. The procedure fine tuned in this study relies from the theoretical standpoint on the procedure defined by Shigeishi and Ohtsu [27]. This procedure, called SiGMA, characterised the AE signal by taking into account only the first arrival time of P-waves.

Based on the generalised theory of acoustic emissions [27], vector $\mathbf{b}(\mathbf{y}, t)$, indicating relative displacement between the two faces of a crack located at point $\mathbf{y}$ at time t, is given by $b(\mathbf{y}) \cdot \boldsymbol{l} S(t)$,where $b(\mathbf{y})$ stands for the amplitude of the displacement, $\boldsymbol{l}$ is the direction vector and $S(t)$ is the function describing the time-dependence of this displacement. The integral of the product of the tensor of the elastic constants C_{pqkl} of the material, the displacement vector $b(\mathbf{y})l_k$, and the vector normal n_l to the surface of the crack, F, leads to the determination of the moment tensor m_{pq}:

$$\int_F C_{pqkl}[b(\mathbf{y})l_k S(t)n_l]\mathrm{d}F = [C_{pqkl}l_k n_l]\Delta V S(t) = m_{pq}S(t). \tag{2}$$

In Eq. (2) ΔV is the volume of the crack, defined as the product of the displacement $b(\mathbf{y})$ and the area of the crack, i.e., $\Delta V = \int_F b(\mathbf{y})\mathrm{d}F$. Thus, the dimension Nm of the moment tensor is given by the elastic constants (N/m^2) times the volume of the crack (m^3). In an isotropic materials, the moment tensor is obtained from the following relationship:

$$m_{pq} = [C_{pqkl}l_k n_l]\Delta V = [\lambda l_k n_k \delta_{pq} + \mu l_p n_p + \mu l_q n_p]\Delta V, \tag{3}$$

where λ and μ are Lamè's constants and δ is Kronecker's delta symbol. The moment tensor m_{pq} is symmetrical in p and q due to the conservation of momentum for an internal source [24], and thus there are six unique moments instead of nine (Fig. 16).

Moreover, the elastic displacements $\mathbf{u}(\mathbf{x}, t)$ at the points $\mathbf{x}$ due to displacement $\mathbf{b}(\mathbf{y}, t)$ which generate the acoustic emission signals are given by:

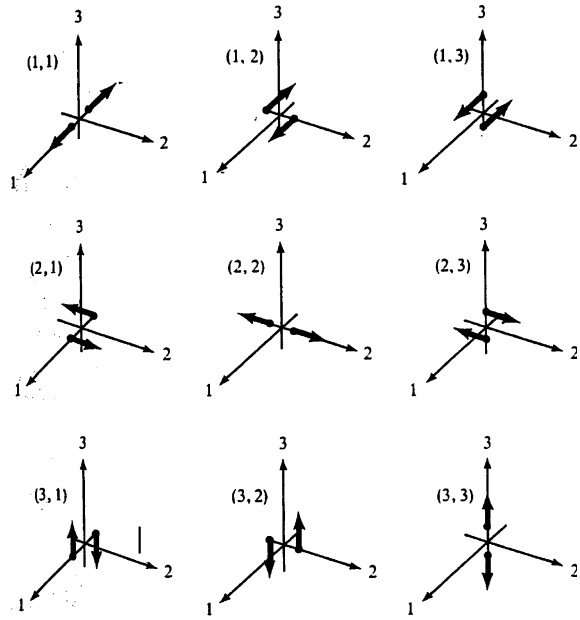

Fig. 16 Nine components of the moment tensor (Aki and Richards [22])

$$u_i(\mathbf{x}, t) = G_{ip,q}(\mathbf{x}, \mathbf{y}, t) m_{pq} * S(t), \quad (4)$$

where, $G_{ip,q}(\mathbf{x}, \mathbf{y}, t)$ is the space derivative of Green's functions and the asterisk denotes the convolution operator. Green's functions describe the elastic displacements $\mathbf{u}(\mathbf{x}, t)$ due to a unit displacement applied in $\mathbf{y}$ at time t. In the SiGMA procedure, the magnitude of the elastic displacements, proportional to the amplitudes $A(\mathbf{x})$ of the first P-waves to reach the transducers, are given by an elaboration of Eq. 4:

$$A(\mathbf{x}) = \frac{C_s\, REF(\mathbf{t}, \mathbf{r})}{R} (r_1\ r_2\ r_3) \times \begin{pmatrix} m_{11} & m_{12} & m_{13} \\ m_{21} & m_{22} & m_{23} \\ m_{31} & m_{32} & m_{33} \end{pmatrix} \begin{pmatrix} r_1 \\ r_2 \\ r_3 \end{pmatrix}, \quad (5)$$

where C_s is a calibration coefficient of the acoustic emission sensors, R is the distance between the AE source at point $\mathbf{y}$ and the sensor located at point $\mathbf{x}$. Vector $\mathbf{r}$ represents the components of the distances, R, obtained through the localisation procedure, and $REF(\mathbf{t},\mathbf{r})$ is the reflection coefficient of the sensitivity of the sensor between vector $\mathbf{r}$ and direction $\mathbf{t}$.

Since the moment tensor is symmetrical, to be able to represent it, it is necessary to determine the six independent unknowns, m_{pq}. To this end, in order to determine the components of the moment tensor, the amplitude of the signal $A(\mathbf{x})$ must be received from at least six AE channels. From an eigenvalue analysis of the moment tensor, it is possible to determine the type of crack localised:

$$\frac{\lambda_1}{\lambda_1} = X + Y + Z, \quad \frac{\lambda_2}{\lambda_1} = 0 - \frac{Y}{2} + Z, \quad \frac{\lambda_3}{\lambda_1} = -X - \frac{Y}{2} + Z \quad (6)$$

where, $\lambda_1, \lambda_2, \lambda_3$ are the maximum, medium and minimum eigenvalues, respectively, X is the component due to shear, Y is the deviatoric tensile component, Z is the isotropic tensile component. Ohtsu classified an AE source with $X > 60\%$ as a shear crack, one with $X < 40\%$ and $Y + Z > 60\%$ as a tensile crack, and one with $40\% < X < 60\%$ as a mixed mode crack [27]. Moreover, from an eigenvector analysis it is possible to determine the versors, $\boldsymbol{l}$ and $\boldsymbol{n}$, which determine the direction of the displacement and the orientation of the crack surfaces [27].

5 Ae monitoring of specimens PS6 and PN4

After repair, masonry test pieces PS6 and PN4 were monitored with the AE technique throughout the loading test. To this end, six PZT transducers were glued with silicone resin to the side faces of the test pieces. These resins are good ultrasound conductors and have the advantage of reducing to the minimum the attenuation of signal perception in the layer between the specimen surface and the applied sensor. To have a truly effective coupling between the specimen and the sensor, it is necessary to make sure that the two surfaces in contact are smooth and clean. A thin layer of glue must be applied so as to fill the gaps and cavities due to the roughness of the surfaces and the air bubbles. The arrangement of the sensors for specimen PN4 is illustrated in Fig. 17, and their positions are listed in Table 4.

The specimens were loaded under strain control imposing constant rate displacement to the upper loading plate. To obtain a very slow crack growth, displacement rates of 8.4×10^{-4} and 6.7×10^{-4} mm/s were adopted for specimens PS6 and PN4 respectively. Load versus time, cumulative AE counting and differential AE counting (for each minute of the testing period) are depicted in Fig. 18. It can be seen that cumulative counts increase, very slowly at first and then proportionally to the load, reaching a peak in the proximity of the highest load reached in each test. The function representing the differential counts (AE count number per minute), instead, reaches its maximum value in the ascending branch of the load-displacement curves and it reduces quickly to nil in the proximity of the ultimate load. From the diagrams of the differential counts of the AE signals, it is therefore possible to identify two phases in the loading process: a first phase during which the biggest cracks are formed and the material reaches a critical damage condition (phase 1), and a second phase during which the material tends to exhaust its bearing capacity (phase 2).

From the diagrams in Fig. 18, it can also be seen that during the tests on the repaired specimen the material begins to release a great quantity of energy once exceeded the maximum stress level reached in the virgin state (point K identified in the load-time curves). In perfect agreement with the so-called *Kaiser effect* [28], these results are useful to assess in

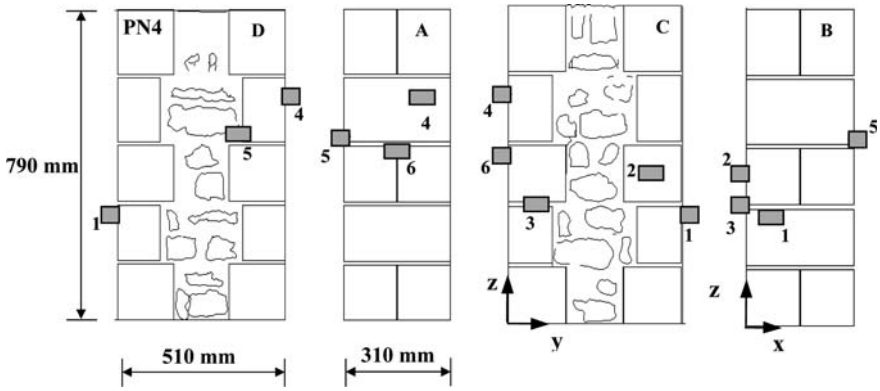

Fig. 17 Arrangement of the PZT sensors on the four side faces of wall PN4

Table 4 Arrangement of the sensors applied to wall PN4

Sensors	x [mm]	y [mm]	z [mm]
*S*1	74	510	284
*S*2	0	417	395
*S*3	0	80	316
*S*4	83	0	502
*S*5	310	150	495
*S*6	15.5	0	417

situ the efficacy of structural strengthening through the AE technique.

Figures 19 and 20 show, on the A and D faces of specimens PS6 and PN4, the projections of the AE sources identified during the loading test.

In particular, during the loading test performed on specimen PS6 (strengthened exclusively with steel rods), 34 AE signal source were identified (Fig. 19). In the localisation process, only the waveforms whose arrival times were recorded almost simultaneously (with differences of the order of microseconds) by the six sensors were used [29]. The moment tensor analysis was also performed on these points. The transmission velocity of the ultrasonic signals through the material was found to be about 1350 m/s, the frequency most often encountered was about 120 kHz. The sources determined during the first phase of the loading test (phase 1) are represented by triangles; the ones determined during phase 2, when the material tends to exhaust its bearing capacity (Table Table 5), are instead represented by squares.

During the load test on specimen PN4 (repaired with grout injections and steel rods), 32 source points were identified from AE signals recorded almost simultaneously by the six sensors (Fig. 20). The transmission speed of the signals was found to be ca 980 m/s, the frequency most often encountered was ca 90 kHz.

The higher speed of the signals in specimen PS6 compared to specimen PN4 should probably be ascribed to the greater compactness of Serena stone versus Noto stone. AE signals, in fact, undergo a considerable attenuation in porous media.

Damage process zone are in good agreement with the considerations expressed in Sect. 3.1. From Fig. 19 it can be seen that in specimen PS6, microcracks are mostly located in the inner leaf, in the zone situated between the two upper braces. A non negligible number of microcracks is also located at the interface between the inner and outer leaves. It should be underscored that virtually all the microcracks identified between the upper braces are located in the tensile zones of the masonry. These zones, according to the diagram in Fig. 14a, are clearly revealed by displacement transducers 13 and 14. Additional microcracks were also identified in the proximity of the zones in tension of the inner leaf by displacement transducers 10 and 12, shown in Fig. 14b.

In specimen PN4, shown in Fig. 20, nearly all the microcracks were identified in the tension zones of the masonry. In this case too, the microcracks were mostly located in the inner leaf, between the two upper braces. According to the diagram in Fig. 15a, these zones were covered by displacement transducers 6 and 2. A certain number of points was also identified in the lower portion of the specimen, and reveal the presence of microcracks in an external Noto stone masonry block.

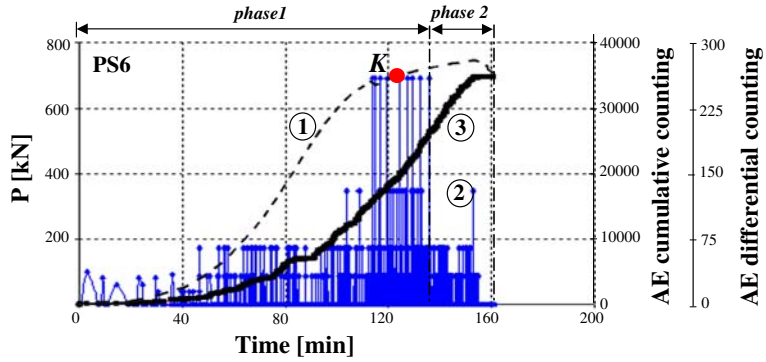

Fig. 18 Loads versus time curves and AE activity for walls PS6 and PN4

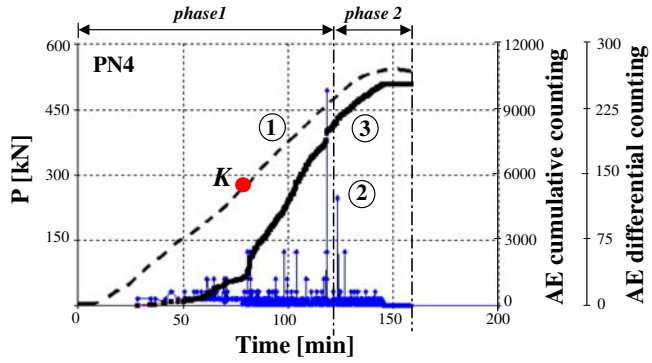

5.1 Estimating the volumes of the microcracks

Shigeishi and Ohtsu [27] pointed out that the trace component of the moment tensor can be expressed with the following relationship, obtained from Eq. 3:

$$m_{kk} = (3\lambda + 2\mu) l_k n_k \Delta V, \tag{7}$$

where λ and μ are Lamè's constants, l_k and n_k are the components of the direction vector and the vector normal to the surface of the crack, m_{kk} is the trace component of the moment tensor and ΔV is the volume expansion of each microcrack.

Furthermore, in connection with the volume expansion of microcracks observed during tests on rock test pieces subject to both uniaxial and triaxial compression, Chang and Lee [30] noted that not all the microcracks localised with the AE technique are always concentrated on visible failure planes during the loading process. As a rule, a group of points situated in the proximity of the cracks is identified. The actual fracture mechanism, visible to the naked eye, can be determined instead from the highest magnitude volume expansion events, which constitute one of the most significant damage indicators.

Similar considerations can be expressed for the testing program described herein.

As a rule, in elasticity theory, factor $(3\lambda + 2\mu) = K$ is considered as a constant specific to each material. Volume expansion may therefore be expressed as follows:

$$\Delta V = \frac{1}{K} \frac{m_{kk}}{l_k n_k}. \tag{8}$$

For specimen PS6 in Serena stone, considering an average elastic modulus $E \cong 20\,000\,\mathrm{N/mm^2}$ and a Poisson coefficient of 0.2 (Table 2), we get $\lambda = Ev/(1+v)(1-2v) \cong 5600\,\mathrm{N/mm^2}$ and $\mu = Ev/2(1-2v) \cong 3300\,\mathrm{N/mm^2}$, which means it is possible to assume an approximate value of $K_s \cong 23\,400\,\mathrm{N/mm^2}$. Similarly, for specimen PN4 in Noto stone, the value of $K_n \cong 10\,500\,\mathrm{N/mm^2}$ can be determined.

Assuming term K to be approximately constant for both specimens throughout the loading tests, it can be seen that the highest magnitude volume expansion

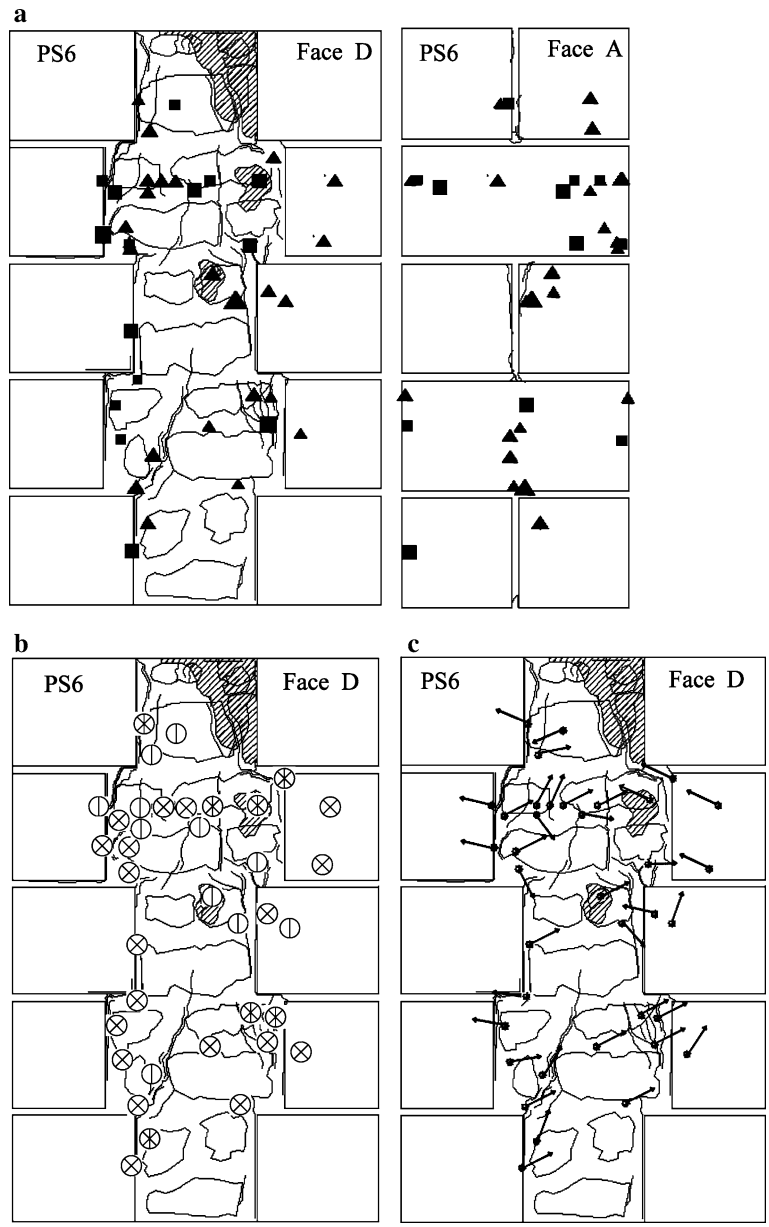

Fig. 19 AE sources in specimen PS6. (**a**) Localisation and magnitudes of crack volumes , (**b**) crack type, (**c**) crack motion vectors

Table 5 Markers of AE sources representing crack volume expansion in the phase 1 and phase 2 of tests and labels identifying crack typology

Phase 1	Phase 2	Crack typology (mode)		
▲	■	⊗	⊖	⊗
$\Delta V \leq 0.1\text{mm}^3$	$\Delta V \leq 0.1\ \text{mm}^3$	shear	tensile	mixed
▲	■			
$0.1 \leq \Delta V \leq 0.2\ \text{mm}^3$	$0.1 \leq \Delta V \leq 0.2\ \text{mm}^3$			
▲	■			
$\Delta V \geq 0.2\ \text{mm}^3$	$\Delta V \geq 0.2\ \text{mm}^3$			

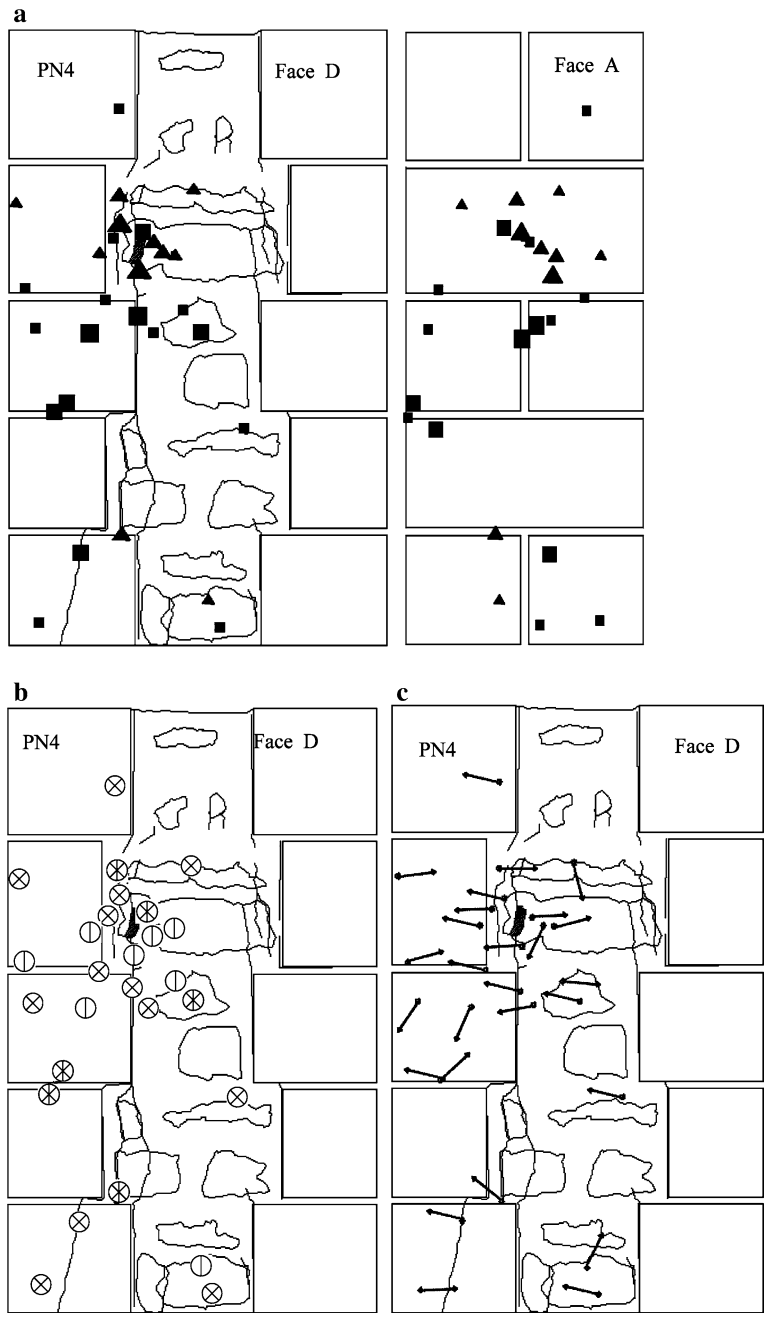

Fig. 20 AE sources in specimen PN4. (**a**) Localisation and magnitudes of crack volumes, (**b**) crack type, (**c**) crack motion vectors

events are concentrated at the macrocracks identified. If the AE sources are identified by means of a graphic representation where individual crack magnitudes are symbolised, an interesting superposition is obtained between the AE sources with large crack volumes and the failure planes visible to the naked eye (Figs. 19 and 20).

For specimens PS6 and PN4, crack volume magnitudes, broken down by loading phase, are represented according to the notation listed in Table 5. Figures 19 and 20 also illustrate crack types, according to the definition given in Sect. 4.2, and the crack motion vectors reflecting the directions of displacement of the fracture surfaces.

5.2 Statistical distribution of AE events

By analogy with seismic phenomena, in the AE field, magnitude is defined as follows:

$$m = \mathrm{Log}_{10} A_{\max} + f(r), \tag{9}$$

where, $A_{\max}$ is the amplitude of the signal expressed in μV, and $f(r)$ is a correction coefficient whereby signal amplitude is taken to be a decreasing function of the distance r between the source and the AE sensor. The reduction in AE signal amplitude in large-sized structures is given by $f(r) = kr$, where r is measured in metres and k corresponds to five magnitudes per metre [31]. In seismology, large magnitude earthquakes occur less frequently than small magnitude ones. This can be quantified through their frequency distributions with the empirical Gutenberg-Richter law [7]:

$$\mathrm{Log}_{10} N(\geq m) = a - bm, \text{ or } N(\geq m) = 10^{a-bm}, \tag{10}$$

where N is the cumulative number of earthquakes with magnitude $\geq m$ in a given area and a specific time-space, whilst b and a are positive constants varying from one region to another. Equation 10 has been used successfully in the AE field to study the scaling laws of AE wave amplitude distribution [6, 32]. This approach highlights the similarity between structural damage phenomena and seismic activities in a given region of the earth, extending the applicability of the Gutenberg-Richter law to Civil Engineering. According to Eq. 10, the "b-value" stands for the slope of the regression line in the "log-linear" diagram of AE signal amplitude distribution. This parameter changes systematically at different times in the course of the damage process and therefore can be used to estimate damage evolution modalities.

Moreover, scale effects on the size of the cracks identified with the AE technique entail, by analogy with earthquakes [6, 7], the validity of the following relationship:

$$N(\geq L) = c\, L^{-2b}, \tag{11}$$

where N is the cumulative number of AE generated by cracks having a characteristic size $\geq L$, c is the total number of AE events and $D = 2b$ is the fractional exponent of the distribution. The cumulative distribution (11) is substantially identical to the one proposed by Carpinteri [8], according to which the number of cracks with size $\geq L$ contained in a body is given by:

$$N^*(\geq L) = N_{\mathrm{tot}}\, L^{-\gamma}. \tag{12}$$

In Eq. (12), γ is an exponent reflecting the disorder, i.e., crack size scatter, and N_{tot} is the total number of cracks contained in the material. By equating distributions (11) and (12), we find that: $2b = \gamma$. At collapse, when the size of the biggest crack is proportional to the characteristic dimensions of a structure, function (12) is characterised by an exponent $\gamma = 2$, corresponding to $b = 1$. In [8] it is also demonstrated that $\gamma = 2$ is a lower limit corresponding to the minimum value $b = 1$, observed experimentally when the bearing capacity of a structural member is exhausted.

By applying these concepts to the analysis of the "b-value" of specimens PS6 and PN4, it can be seen that the former exhausted its bearing capacity during the load test, with the formation of cracks of a size comparable to that of the specimen, forming along the interface between the filler and the outer wall (b-value $\cong 1$), and the latter, characterised by a widespread cracking pattern, still has a reserve of strength before reaching the final collapse (b-value $\cong 1.7$). The determination of the "b-values" for the two specimens is shown in Fig. 21.

6 Conclusions

An experimental research has been carried out on three-leaf walls built using two stones having different characteristics, and according to two geometric patterns, so as to reproduce the masonry types commonly used in Italian historical centres. After

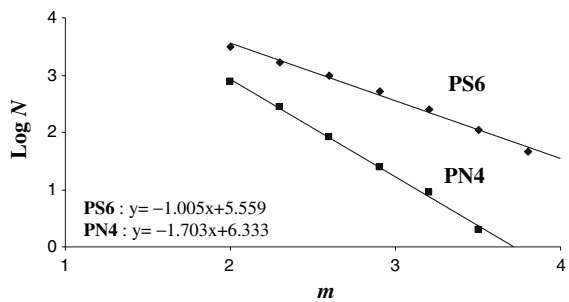

Fig. 21 Determination of the "b-value" at the end of the loading test on the two specimens

shear testing, some specimens could be recovered and repaired by grout injection and steel rods confinement. The subsequent shear tests carried out on the repaired specimens made it possible to assess the effectiveness of the techniques adopted. A higher load increase was achieved in the case of the wall repaired with both techniques; the use of grouting only resulted into a stiffer and more brittle behaviour, whereas in the case of steel rods only a particularly ductile behaviour was observed.

Laboratory tests were performed with the aid of an advanced equipment for the acquisition and processing of AE signals. The damage process zones, identified in the specimens with the AE technique, were in good agreement with the results of the experimental analysis performed by means of displacement transducers.

Finally, by adopting statistical techniques combined with AE monitoring, similar to the techniques used by seismologists in assessing earthquake frequency distributions—Gutenberg-Richter (GR) law—it proved possible to gain an understanding to the relationships linking macrocracking events and the macroscopic behaviour entailing a loss of structural bearing capacity. Thus, test results show that, where a structure is monitored by means of the AE technique, the control of the "*b*-value", suggested by the GR law, conducted jointly with microcrack localisation, is particularly useful for the identification of the critical state which may result in the loss of bearing capacity of a structure of a part thereof.

Acknowledgements The authors gratefully acknowledge the assistance provided by M. Brazzale, I. Mecca and S. Rampoldi in the experimental activities, M. Antico and M. Iscandri for the technical support received.

References

1. Binda L, Anzani A, Fontana A (2003) Mechanical behaviour of multiple-leaf stone masonry: experimental research. 3-Day International Conference on Structural Faults & Repair, London, 1–3 July 2003, MC Forde (ed) Engineering Technics Press, Edinburgh, ISBN 0-947644-53-9, CD-ROM, Keynote Lecture
2. Binda L, Fontana A, Anzani A (2003) Multi-leaf Masonry: shear transfer at interfaces, 6th International Symposium on Computer Methods in Structural Masonry (STRUMAS VI), Ed. TG Hughes & G N Pande Computers & Geotechnics Ltd, ISBN 0-9510380-3-6, Roma 22–24 September 2003, pp 142–148
3. Carpinteri A, Lacidogna G (2006) Damage monitoring of an historical masonry building by the acoustic emission technique. Mater Struct 20:143–149
4. Carpinteri A, Lacidogna G, Pugno N (2004) A fractal approach for damage detection in concrete and masonry structures by acoustic emission technique. Acoustique et Techniques 38:31–37
5. Carpinteri A, Lacidogna G, Pugno N (2007) Structural damage diagnosis and life-time assessment by acoustic emission monitoring. Eng Frac Mech 74:273–289
6. Carpinteri A, Lacidogna G, Niccolini G (2006) Critical behaviour in concrete structures and damage localization by acoustic emission. Key Eng Mater 312:305–310
7. Richter CF (1958) Elementary seismology. W.H. Freeman and Company, S Francisco and London
8. Carpinteri A (1994) Scaling laws and renormalization groups for strength and toughness of disordered materials. Int J Solids Struct 31:291–302
9. Anzani A, Binda L, Fontana A, Pina-Henriques J (2004) An experimental investigation on multiple-leaf stone masonry. Paper presented at 13th International Brick/Block Masonry Conference RAI Amsterdam, 4–7 July 2004
10. Hendry AW (1981) Structural brickwork. Mac Millan Press, London
11. Baronio G, Tedeschi C, Binda L (2001) Restoration of a tower: choice of mortars and grouts for repointing and injection, 9th International Conference and Exhibition on Structural Faults + Repair, 4–6 July 2001
12. Van Rickstal F, Toumbakari E, Ignoul S, Van Gemert D (2003) Development of mineral grouts for consolidation injection. Adv Mater Sci Restor AMSR 1:61–76
13. Toumbakari E, Van Gemert D, Tassios TP, Vintzileou E (2003) Effect of the mechanical properties of injection grouts on the structural behaviour of three-leaf walls. Proceedings of the 9th North American Masonry Conference
14. Van Gemert D, Ignoul S, Van Rickstal F (2003) Structural consolidation and strengthening of ancient masonry: grout development and case-studies. Proceedings of the 2nd International Conference on Conservation of Monuments, Lucknow, India, 18–19 October 2003
15. Schueremans L (2003) Evaluation of bearing capacity and design of consolidation and strengthening by means of injections. Seminar: Structural Consolidation, MSR VI, Materials Science and Restoration, Karlsruhe, Germany, September 16–18 2003
16. Modena C, Valluzzi MR, Tongini Folli R, Binda L (2002) Design choices and intervention techniques for repairing and strengthening of the monza cathedral bell-tower. Construct Build Mater 16(7):385–395, ISSN 0950-0618, Special Issue
17. Vogel T, Köppel S (2003) Possibilities and limitations of acoustic emission analysis for reinforced concrete. International Symposium on Non-Destructive Testing in Civil Engineering (NDT-CE 2003), Berlin, September 2003
18. Landis EN, Shah SP (1995) Frequency-dependent stress wave attenuation in cement-based materials. J Eng Mech 121:737–743
19. Köppel S, Grosse C (2000) Advanced acoustic emission techniques for failure analysis in concrete. Proceedings of the 15th World Conference on Non-Destructive Testing, Rome, Oct. 2000, CD-ROM, Paper N. 231

20. Shah SP, Li Z (1994) Localization of microcracking in concrete under uniaxial tension. ACI Mater J 91:372–381
21. Carpinteri A, Lacidogna G, Niccolini G (2005) Crack localisation in a large-sized R.C. beam through the acoustic emission technique. Proceedings of the 17th National Congress of Theoretical and Applied Mechanics (AIMETA), Florence, CD-Rom, Paper N. 23
22. Aki K, Richards PG (1980) Quantitative seismology, theory and method, 2nd ed. University Science Books, Sausalito CA
23. Ohtsu M, Ono K (1984) A generalized theory of acoustic emission and Green's functions in half space. J Acoust Emis 3:124–133
24. Maruyama T (1963) On force equivalents dynamic elastic dislocations with reference to the earthquake mechanisms. Bull Earthquake Res Inst Univ Tokyo 41:467–486
25. Carpinteri A, Lacidogna G, Paggi M (2006) Acoustic emission monitoring and numerical modelling of FRP delamination in RC beams with non rectangular cross-section. Mater Struct 40:553–566
26. Schubert F, Schenninger B (2002) Numerical modelling of acoustic emission sources and wave propagation in concrete. NDT.net e-J Nondest Test 7(9)
27. Shigeishi M, Ohtsu M (2001) Acoustic emission moment tensor analysis: development for crack identification in concrete materials. Construct Build Mater 15:311–319
28. Kaiser J (1950) An investigation into the occurrence of noises in tensile tests, or a study of acoustic phenomena in tensile tests. Ph.D, Technische Hochschule München, Munich FRG
30. Shah SP, Li Z (1994) Localisation of microcracking in concrete under uniaxial tension. ACI Mater J 91:372–381
31. Chang SH, Lee CI (2004) Estimation of cracking and damage mechanisms in rock under triaxial compression by moment tensor analysis of acoustic emission. Int J Rock Mech Mining Sci 41:1069–1086
32. Uomoto T (1987) Application of acoustic emission to the field of concrete engineering. J Acoustic Emis 6:137–144
33. Colombo S, Main IG, Forde MC (2003) Assessing damage of reinforced concrete beam using "*b*-value" analysis of acoustic emission signals. J Mater Civil Eng ASCE 15:280–286